DETERMINING NIGHTTIME ATMOSPHERIC OPTICAL DEPTH USING MARS EXPLORATION ROVER IMAGES

A Thesis

by

KERI MARIE BEAN

Submitted to the Office of Graduate Studies of
Texas A&M University
in partial fulfillment of the requirements for the degree of

MASTER OF SCIENCE

Chair of Committee,	Mark Lemmon
Committee Members,	David Sparks
	Istvan Szunyogh
Head of Department,	Ping Yang

August 2013

Major Subject: Atmospheric Science

ABSTRACT

Martian clouds and dust play an important part of the radiative transfer and energy balance budget. To assist in fully understanding the impact of clouds and dust, the complete diurnal cycle needs to be characterized. One of the best methods to track diurnal variations on Mars is by measuring optical depth. The spatial and temporal trends of optical depth give insight into the dust and water cycles of the Martian atmosphere.

Until now, spacecraft could only obtain optical depth during the day. In this thesis, nighttime images from the Mars Exploration Rover *Spirit* are used to calculate nighttime optical depth using photometric methods to capture star flux. Bright stars in well-known constellations are used in this analysis. The observed flux was compared to the expected flux to give nighttime optical depth values. The observed nighttime optical depth was consistently similar to the daytime optical depth values on both an individual image and sol-averaged basis.

Recommendations are made going forward to use the Mars Science Laboratory *Curiosity* for conducting an optimal nighttime optical depth campaign to fully characterize the diurnal dust and water cycles of Mars. The *Curiosity* rover is well suited for nighttime imaging and can potentially provide valuable insight into the nighttime dust and cloud trends.

DEDICATION

This thesis is dedicated to my husband Jeffrey McGee and our cats Mindy and Misty.

ACKNOWLEDGEMENTS

First and foremost, I would like to thank and acknowledge my advisor Dr. Mark Lemmon. I began working for him in the fall of 2007 when I started as a freshman at Texas A&M University. Without him, I would not have had an exhilarating college career. We've survived EDL and Mars time twice together, and that is a bond not easily forgotten. He has shown me the wonders of planetary science and guided me to become a strong and resourceful scientist.

I would also like to thank the other members of my committee, Dr. Istvan Szunyogh and Dr. David Sparks. I appreciate their support. I would also like to send extra thanks to Dr. Sparks for teaching a great planetary geology class and letting me crash the freshman seminar series Mars class.

Of course, I would like to thank my husband Jeffrey McGee. Jeff has been extremely patient and caring of me, especially with the many hurdles that we have faced so far. I'll also extend a scratch of the ear to our cats, Mindy and Misty, for without them I surely would be less cuddled and happy. All three deserve extra love for dealing with me being at JPL for three months of Mars time and surviving.

I'd like to thank my parents, Thomas and Tracy Bean, my brother Kevin Bean, and my grandfather Martin McKinley for being supportive of me throughout the years.

I could go on listing friends forever, but I would like to thank them for being awesome and supportive. In particular, I'd like to thank Nicole Sharp, Bonnie Stern, Rita Matos, Ryan Michaels, and Carleen DeArmon.

I would also like to thank all of my fellow Phoenix Mars Lander and Mars Science Laboratory colleagues. I am extremely privileged to be part of such a special group of people. In particular, I'd like to thank the ladies like Laurie Leshin, Aileen Yingst, Linda Kah, Michelle Minitti, Dawn Sumner, and many more for being awesome role models and amazingly supportive.

I've had a slew of great teachers throughout the course of my life. Many thanks to all of them!

And finally, thanks to Texas A&M University for a fun six years in Aggieland.

NOMENCLATURE

B-V	Blue and Visual Magnitude Difference
BSL	Bright Star List
CCD	Charge Coupled Device
ChemCam	Chemical Camera, Instrument on Mars Science Laboratory
DN	Data Number
η	Airmass
F	Flux
F_e	Expected Flux
F_o	Observed Flux
$F_{o,er}$	Observed Flux Error
FR	Flux Ratio
$\underline{FR}$	Weighted Average of the Flux Ratios
FR_{er}	Flux Ratio Error
FR_0	Flux Ratio at Zero Airmass
$FR_{0,er}$	Flux Ratio at Zero Airmass Error
GCM	General Circulation Model
HRSC	High Resolution Stereo Camera, Instrument on Mars Express
IN	Intercept From the Linear Fit
IDL	Interactive Data Language
IFOV	Instantaneous Field of View

K	Kelvin
L1	Left Eye #1 Filter on Pancam
LIBS	Laser-Induced Breakdown Spectrometer, part of ChemCam
LIDAR	Light Detection and Ranging, Instrument on Phoenix Mars Lander
LTST	Local True Solar Time
Mastcam	Mast Camera, Main Cameras on Mars Science Laboratory
MER	Mars Exploration Rover
MGS	Mars Global Surveyor
MOC	Mars Orbiter Camera, Instrument on Mars Global Surveyor
MOLA	Mars Orbiter Laser Altimeter, Instrument on MGS
MSL	Mars Science Laboratory
Pancam	Panoramic Camera, Main Cameras on Mars Exploration Rovers
PDS	Planetary Data System
PFS	Planetary Fourier Spectrometer
REMS	Rover Environmental Monitoring System, Instrument on MSL
RMI	Remote Micro Imager, Part of ChemCam
σ	Standard Deviation
$\sigma_{\tau,N}$	Nighttime Optical Depth Error
$\sigma_{\tau,N,tot}$	Total Accumulated Nighttime Optical Depth Error
Sol	Martian Day, Counted up From Date of Landing
T_{eff}	Effective Temperature
τ	Daytime Optical Depth

τ_N	Nighttime Optical Depth
$\underline{\tau}_{sol}$	Sol-Averaged Nighttime Optical Depth
θ	Star Elevation Angle
V	Visual Magnitude Filter

TABLE OF CONTENTS

Page

LIST OF FIGURES

LIST OF TABLES

CHAPTER I

INTRODUCTION

Overview

Mars has been under study for generations. Spacecraft have been sent to Mars to fly by, to orbit, to land, and to rove starting in the 1960s. Telescopes have been aimed at Mars for centuries. This combination of spacecraft and telescope observations has resulted in a wealth of images and meteorological sensor information to help understand the meteorological processes and radiative transfer processes of Mars.

Mars has a dynamic atmosphere with active weather patterns (Cantor et al., 2002). Clouds have been observed on Mars for decades (Smith and Smith, 1972). Clouds are a fundamental part of the water cycle and need to be well characterized to understand radiative transfer and energy transport within the atmosphere (Montmessin et al., 2004; Rodin et al., 1999). The atmospheric dust also plays a vital role in the energy balance of Mars, acting against the greenhouse effect of the mostly carbon dioxide atmosphere (Haberle and Jakosky, 1991).

The Martian Atmosphere

The Martian atmosphere is thin and tenuous compared to Earth's atmosphere, with less than 1% of the Earth's atmospheric pressure. Mars' atmosphere is primarily

composed of carbon dioxide. Water vapor and condensates have been known for decades, but exist in such small quantities that the water has little of a dynamical or energetic role.

Dust storms and other weather phenomena have been observed on Mars for decades using many different spacecraft and ground-based telescopes. Local and regional dust storms (Fig. 1) are common each Mars year (Malin et al., 2008, 2010). Global dust storm events (Fig. 2) were observed from Earth and then confirmed by the *Mariner 9* spacecraft in the 1970s and have occurred occasionally since then (Hanel et al., 1972; Toon et al., 1977).

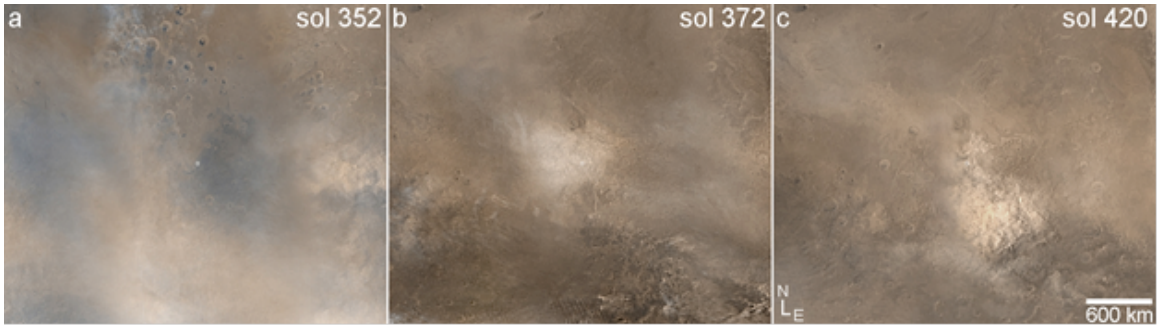

Figure 1: Dust Storm Activity. These are examples of dust storm activity at the sites of the Mars Exploration Rovers. The left image was taken on December 31, 2004 of Meridiani Planum, where *Opportunity* is located. The center and right images are of Gusev Crater, where *Spirit* is located, on January 19, 2005 and March 9, 2005 respectively. The images are stretched to provide detail and contrast. Image credit: NASA/JPL/Malin Space Science Systems. Figure is from Lemmon et al., 2013.

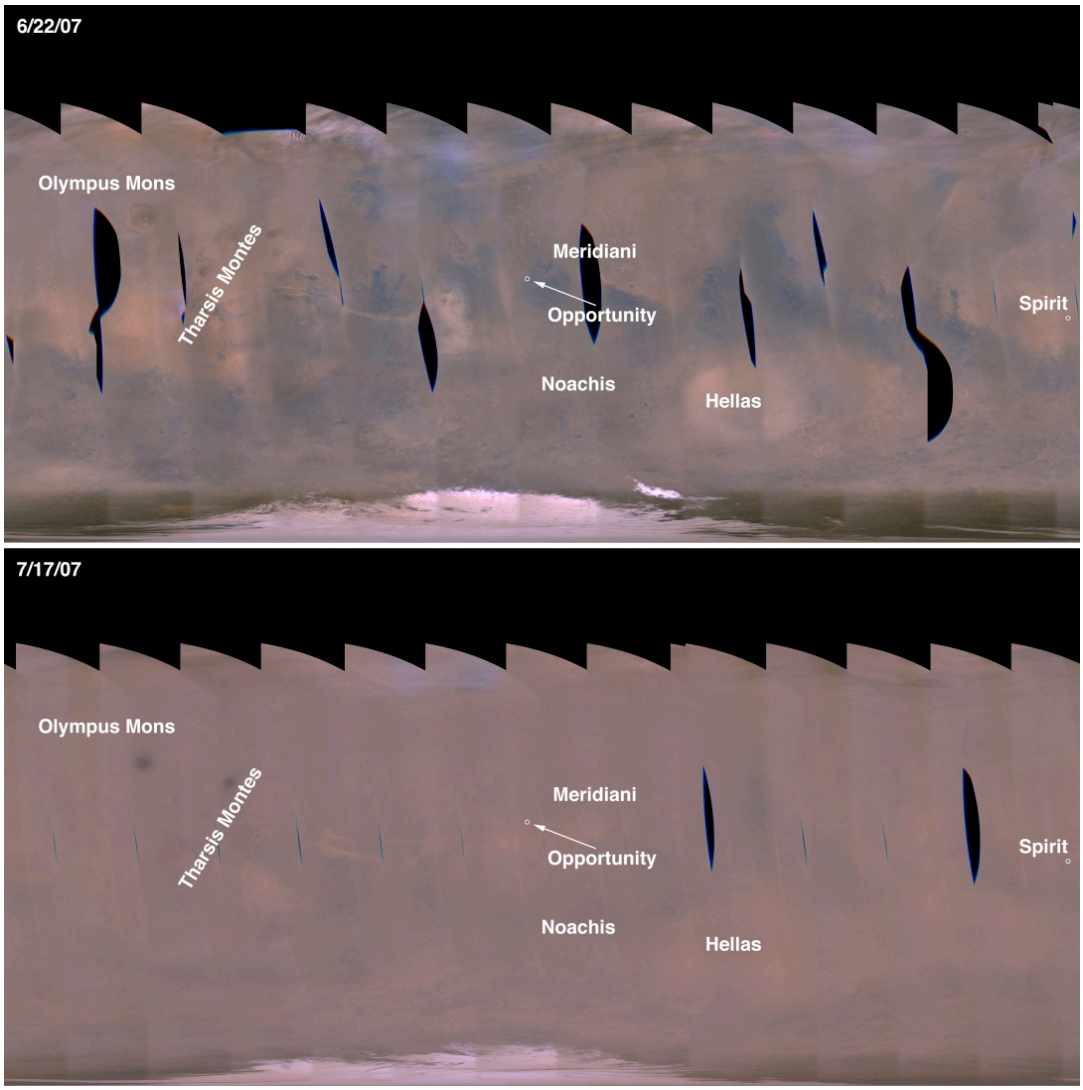

Figure 2: 2007 Global Dust Storm. This is an image of the global dust storm that occurred around sol 1270 of *Spirit*'s mission. Major Martian features are labeled, along with Mars Exploration Rovers *Spirit* and *Opportunity*'s location. Image credit: NASA/JPL/Malin Space Science Systems. This figure is from Lemmon et al., 2013.

Clouds on Mars

Atmospheric imaging from Mars extends back to the *Viking* spacecraft in the 1970s, when the *Viking* landers took images of the sky just after sunset and just before sunrise, as well as measuring direct solar flux. This imaging campaign found a higher

morning optical depth that was attributed to condensed water, likely in ice phase (Colburn et al., 1988). *Viking 2* also imaged frost during its winter (Svitek and Murray, 1990). The thin layer of frost was a combination of water and carbon dioxide in ice phase, condensed onto dust particles brought to the *Viking 2* site by a dust storm (Wall, 1981).

The *Mars Pathfinder* mission provided consistent daytime and occasional nighttime atmospheric optical depth (Smith and Lemmon 1999; Thomas et al., 1999). The nighttime images from *Mars Pathfinder* showed a possibly higher nighttime optical depth than daytime optical depth. The hypothesis behind the higher nighttime optical depth is that water ice crystals were forming in the atmosphere (Thomas et al., 1999). Figure 3 shows an image of twilight clouds observed by *Mars Pathfinder.*

Figure 3: Twilight Clouds as Seen by *Mars Pathfinder*. This image was taken on sol 15. Image credit: NASA/JPL

Observations from the James Clerk Maxwell Telescope on Mauna Kea, Hawaii in the late 1990s indicated a very cold Martian mesosphere. The mesospheric temperature was within 10 to 15K of the carbon dioxide vapor saturation temperature, which implied the formation of local carbon dioxide ice clouds due to local instabilities and perturbations. These observations were correlated with *Mars Pathfinder* and *Viking* data for images of carbon dioxide ice clouds (Clancy and Sandor, 1998).

The *Mars Global Surveyor* orbiter monitored Martian water ice clouds from orbit over several Mars years and found that during perihelion, the atmosphere is relatively free of water ice clouds but warm and dusty. Aphelion was relatively cloudy and cooler with less atmospheric dust (Smith, 2004).

The *Phoenix* lander used a Light Detection and Ranging (LIDAR) instrument at night. These LIDAR observations verified clouds and water ice precipitation in the north polar region of Mars (Whiteway et al., 2009). *Phoenix*'s Surface Stereo Imager was used to complement the LIDAR operations and observed near-surface fog (Moores et al., 2011).

The *Mars Express* orbiter has directly imaged fog (Fig. 4) with the High Resolution Stereo Camera (HRSC). Concurrent observations by the *Mars Express* Planetary Fourier Spectrometer (PFS) indicated the fog is composed of water ice and not carbon dioxide ice. Also, fog has been observed at tropical and equatorial latitudes at low altitude sites (Möhlmann et al., 2009).

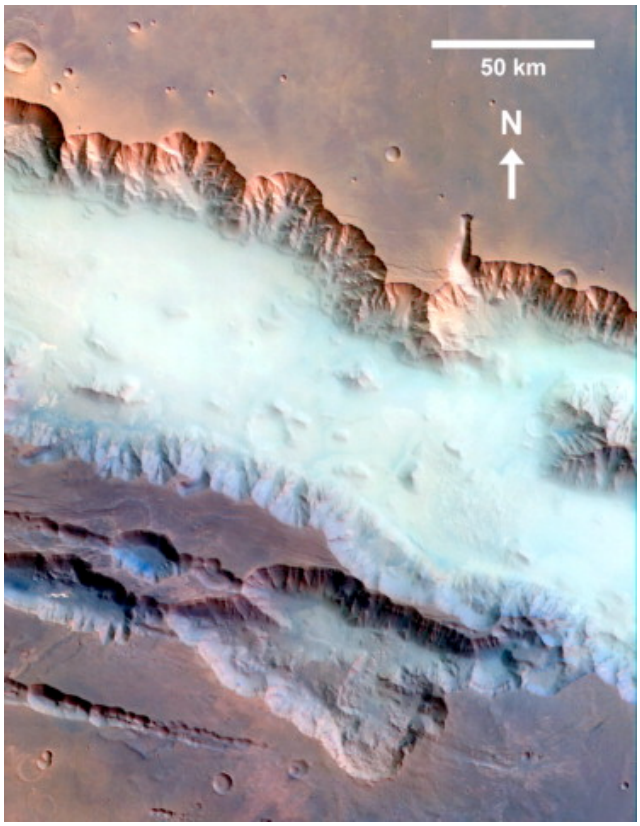

Figure 4: Morning Fog in Valles Marineris. This is an image by the *Mars Express* HRSC taken at 09:20 local true solar time (LTST). This figure is from Möhlmann et al., 2009.

Mars general circulation model (GCM) runs suggest the presence of water ice clouds at night as a result of radiative cooling, with a peak in equatorial and tropical water ice clouds between the northern summer solstice and northern autumnal equinox (Richardson et al., 2002). In a different Mars GCM run, the Martian tropics, especially in the Tharsis and Arabia regions, were identified as having anomalously warm surface temperatures during the night. The surface temperature was shown to be higher by several degrees. This temperature anomaly correlated closely with the aphelion cloud belt. The thermal anomaly was determined to be the result of nighttime water ice clouds forming and trapping infrared radiation, thus keeping the surface warmer than expected.

The optical depth was found to be approximately 1, which implied thicker and more extensive nighttime clouds than daytime clouds. This model result agrees closely with atmospheric extinction data from the Mars Orbiter Laser Altimeter (MOLA) (Wilson et al., 2007).

Optical Depth

Atmospheric optical depth is a dimensionless measure of extinction that describes the amount of radiation that is absorbed and scattered as the radiation travels through the atmosphere. The radiation can interact with aerosols and gases during its traverse through the atmosphere. An optical depth of 0 indicates an atmosphere with no scattering or absorption of radiation. For aerosols with given physical properties, optical depth increases in proportion to their mass loading in the atmosphere, and it is useful as a proxy for that quantity. Optical depth itself can be measured by determining extinction relative to incident flux.

Spatial and temporal variations in optical depth can reveal a lot about atmospheric conditions. From atmospheric optical depth patterns, the presence of water ice clouds, aerosol concentrations, and other meteorological events can be derived. Atmospheric optical depth is influenced by aerosol size and concentration. Optical depth also varies over the electromagnetic spectrum.

Optical depth monitoring can be used to provide constraints on the Martian dust and water cycles. Dust cycle characterization is fundamental for understanding radiative

transfer, energy transport, and scattering within the atmosphere (Kahn et al., 1992). The amount of dust in the atmosphere affects optical depth. Dust settling out decreases optical depth since there would be fewer aerosols present to scatter the incoming radiation. Water ice clouds would increase optical depth, since clouds are very effective at scattering incoming radiation. The daytime dust and water cycle components are now well characterized due to the efforts of multiple Mars missions (Smith and Lemmon, 1999; Smith et al., 2001; Lemmon et al., 2004; Lemmon et al., 2013). Nighttime atmospheric dust and water characteristics are not well constrained due to the spacecraft having difficulties in obtaining nighttime information.

Spirit & *Opportunity* – The Mars Exploration Rovers

The Mars Exploration Rover *Spirit* operated in Gusev Crater, Mars, from January 4, 2004 to March 22, 2010. Gusev Crater is in the southern tropical region of Mars, which makes it an optimal location to observe the aphelion cloud belt. The Mars Exploration Rover *Opportunity* landed in Meridiani Planum, Mars, on January 25, 2004, and it is currently still in operation as of this writing. Meridiani Planum is in the equatorial region of Mars. Both rovers are solar-array powered missions. The purpose of the Mars Exploration Rovers was to explore their respective landing sites for evidence of past surface water.

Gusev Crater, where *Spirit* landed, is an extremely active dust devil area. Dust devils are responsible for a significant amount of the dust load into the atmosphere

(Greeley et al., 2006). Dust devils were imaged multiple times over the course of *Spirit*'s mission (Fig. 5). Dust devils are not expected in a nighttime setting due to the need of solar flux to create the instabilities required for dust devil formation and activity.

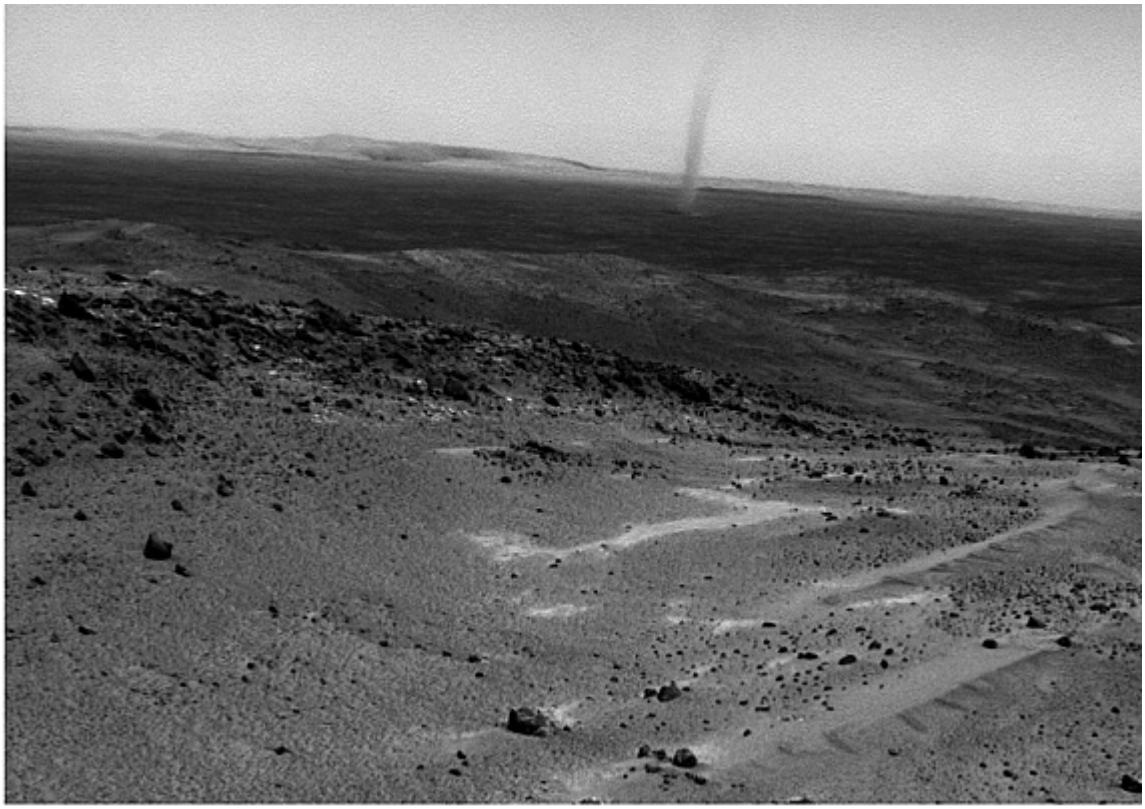

Figure 5: Dust Devil Seen by *Spirit.* Example of a dust devil imaged in Gusev Crater by *Spirit*. This dust devil was imaged on sol 616. The contrast is stretched in this image to provide more details. This figure is from Greeley et al., 2006.

Spirit and *Opportunity* have both imaged water ice daytime clouds associated with the seasonal aphelion cloud belt (Fig. 6) (Lemmon et al., 2004). No twilight clouds were reported during the 90 sol primary mission (Bell et al., 2004). However, twilight clouds have been imaged in the extended mission, including at times close to images used for nighttime optical depth measurements (Fig. 7).

Figure 6: Clouds as Seen by *Opportunity.* This image was taken on sol 269. Image Credit: NASA/JPL.

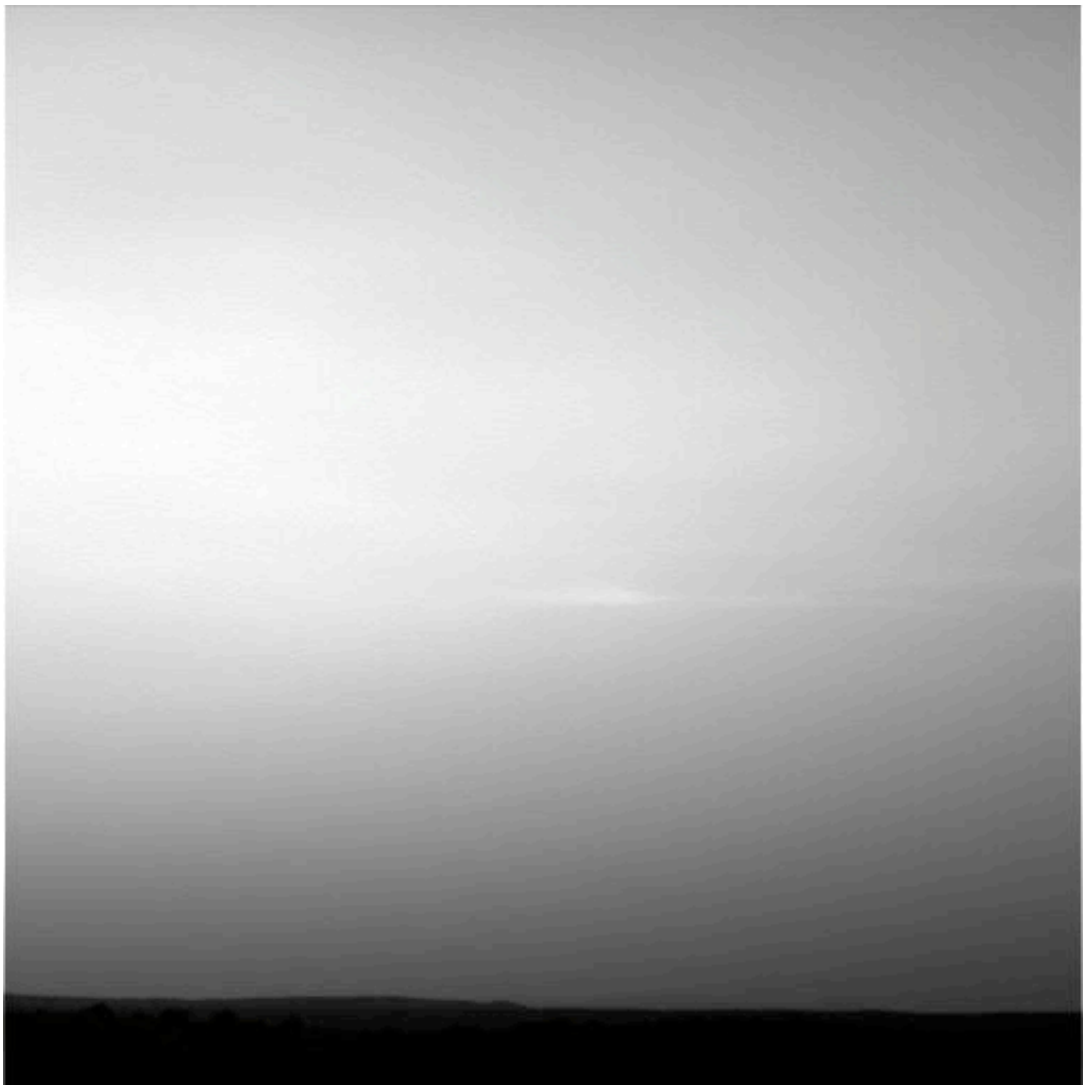

Figure 7: Twilight Clouds as Seen by *Spirit.* This image was taken on sol 1976; just days after images were used for nighttime optical depth measurements. Image Credit: NASA/JPL

During part of the mission, *Spirit* conducted a nighttime imaging campaign. Images included stars, Martian moons, and planets. Most nighttime star images were taken as part of a fruitless meteor search (Domokos et al., 2007). The images were all taken during the southern hemispheric summer, due to energy availability and the thermal constraints of the rover. *Spirit* had to use the energy at night to avoid

overheating from either energy use or thermal shunting of excess power during the day. Due to the constraints on solar power and heating requirements during other seasons, nighttime images could generally not be obtained.

Unfortunately, *Opportunity* has a heater problem that requires the battery to be shut off at night. Thus, *Opportunity* has not acquired any data that is useful for nighttime optical depth campaigns. Going forward, all data analysis mentioned will be from images that *Spirit* has taken.

In this thesis, I used this opportunistic nighttime imaging data set to look for nighttime cloud and condensate development by measuring atmospheric extinction and looking for any resulting optical depths in excess of the daytime optical depth values. This determines whether the predicted nighttime clouds are occurring during the time of these images. To determine nighttime atmospheric optical depth, the observed flux signals from the stars in these opportunistic nighttime images were compared to the known magnitudes of the stars.

In Chapter 2, I will discuss the images used to obtain nighttime optical depth. The limitations of using Pancam for nighttime optical depth purposes and image data availability are also presented. Chapter 3 focuses on the analysis process of the nighttime images to obtain useful nighttime optical depth measurements. The methods of reading and calibrating data, star identification, obtaining flux, the reasoning behind rejecting some stars, and the process of calibrating the flux are discussed in depth. In Chapter 4 I discuss the comparison between the daytime and nighttime optical depth, discuss any potential small-scale variability, and many of the lessons learned for future missions.

The final chapter includes the conclusions from the data, proving that this method is valid for obtaining nighttime optical depth measurements, the results of the sol-averaged nighttime optical depth and individual image nighttime optical depths, and how *Curiosity* will be able to help constrain any condensate formation and nighttime optical depth trends.

CHAPTER II

OBSERVATIONS

The Pancam Instrument

For the nighttime atmospheric imaging campaigns, the Pancam instrument was used. Pancam, short for panoramic camera, is a stereo camera with multiple filters to allow for multispectral color imaging via sequential exposures. Pancam is useful for a wide range of geological and meteorological purposes (Bell et al., 2003). Pancam's active sensor array is a 1 Megapixel Charge Coupled Device (CCD). Pancam has a 16 degree field of view and 0.27 milliradian instantaneous field of view (IFOV, or pixel scale). At f/20, Pancam can be considered to be a "slow" camera.

Images at night were taken in multiple filters for various purposes, but the only useful data for nighttime optical depth measurements came from the left eye's #1 filter (L1) images. The L1 filter has an effective wavelength of 739 nm and a large bandpass covering nearly all visible light and some near infrared (Bell et al., 2003). Pancam is capable of up to five minute exposures, but remains stationary when imaging. Thus the sensitivity is limited by the fact that stars trail across the CCD at a rate of approximately one pixel every four seconds.

Pancam's sensor is a frame transfer CCD. There is not a physical shutter. On CCD readout, the image is shifted from an active area to an aluminum-coated inactive area within approximately five milliseconds, and the readout is conducted over several

seconds. An electronic bias is applied to the analog-to-digital converter so that at any temperature, the readout voltage is positive. One data number (DN) in the digital output corresponds to about 30 electrons in a pixel. Given the CCD quantum efficiency, this would be equal to approximately 100-150 photons striking the detector. For this study, I used raw Pancam data. If necessary, they were rescaled from an 8-bit square root encoded data set back to a linear (flux proportional to DN) set on input. Planetary Data System (PDS) archived radiance calibrated images were not used, since they included dark subtraction followed by truncation of negative values. Thus in the event of oversubtraction, an event with a statistical 50% likelihood, a zero value could have corresponded to a -1 or -10 DN. That process made a true dark-current background subtraction imprecise.

Images in Data Set & Acquisition

Pancam was designed for bright daytime scenery imaging. The stars imaged are point sources for the CCD, so longer exposures – to gain enough signal over the background noise - created star trails. Figure 8 gives an example of unprocessed nighttime star trail images at multiple exposure lengths. The longer exposures, while allowing for better star detection, have the disadvantage of allowing cosmic ray interference. Some cosmic rays are nearly indistinguishable from stars at a glance, so the images were paired with a background image of the same star field taken within the

same observation set. This allowed obvious star trails to continue between two images, and anomalous cosmic rays to be discounted.

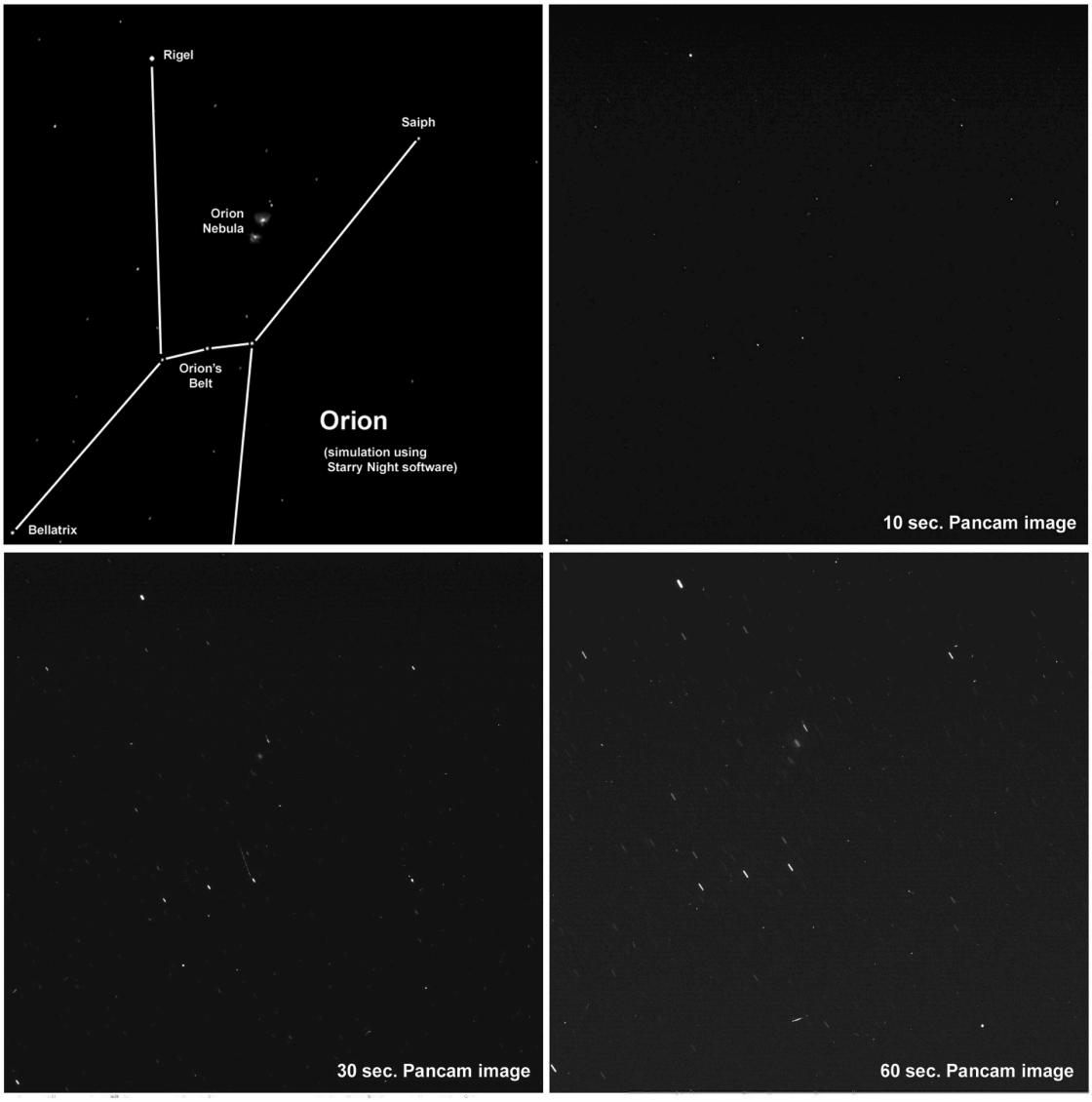

Figure 8: Raw Nighttime Images of Orion. This is an example of the raw images of star fields used for nighttime optical depth measurements. The top left corner is a computer simulation by the Starry Night software showing the Pancam field of view. The other panels are actual, unprocessed images at various exposure lengths. Image credit: NASA/JPL/Cornell.

Many images were paired with a right eye exposure to allow for identification of especially bright meteors as distinct from cosmic rays. However, in Domokos et al., 2007, the distribution of the non-star sources was consistent with only cosmic rays. The needs of the meteor campaign dominated the choice of timing and star fields. Most of the nighttime images were taken near the time of a predicted meteor shower, and in or near the direction of the radiant of the respective meteor shower (Fig. 9). Some of the rest were taken as part of a non-successful search for a Phobos dust torus (Mark Lemmon, personal communication, 2013).

Around *Spirit* sol 1270, there was a global dust storm that led to a significant deposition of dust onto the Pancam lenses. This reduced the response of the camera by up to 60 DN, but bright stars were still visible.

Star field observations chosen for optical depth calculations consisted of a minimum of two images close in time. Most observations occurred within a half hour time period at various times throughout the night. Images with exposures shorter than eight seconds were not used due to the difficulty in getting a good signal-to-noise ratio in many stars. Exposures of three to five minutes, taken as part of a search for a dust torus around Mars, were not always used in analysis due to the density of cosmic rays in the images. In total, 13 nights were useful for obtaining nighttime optical depth information (Table 1).

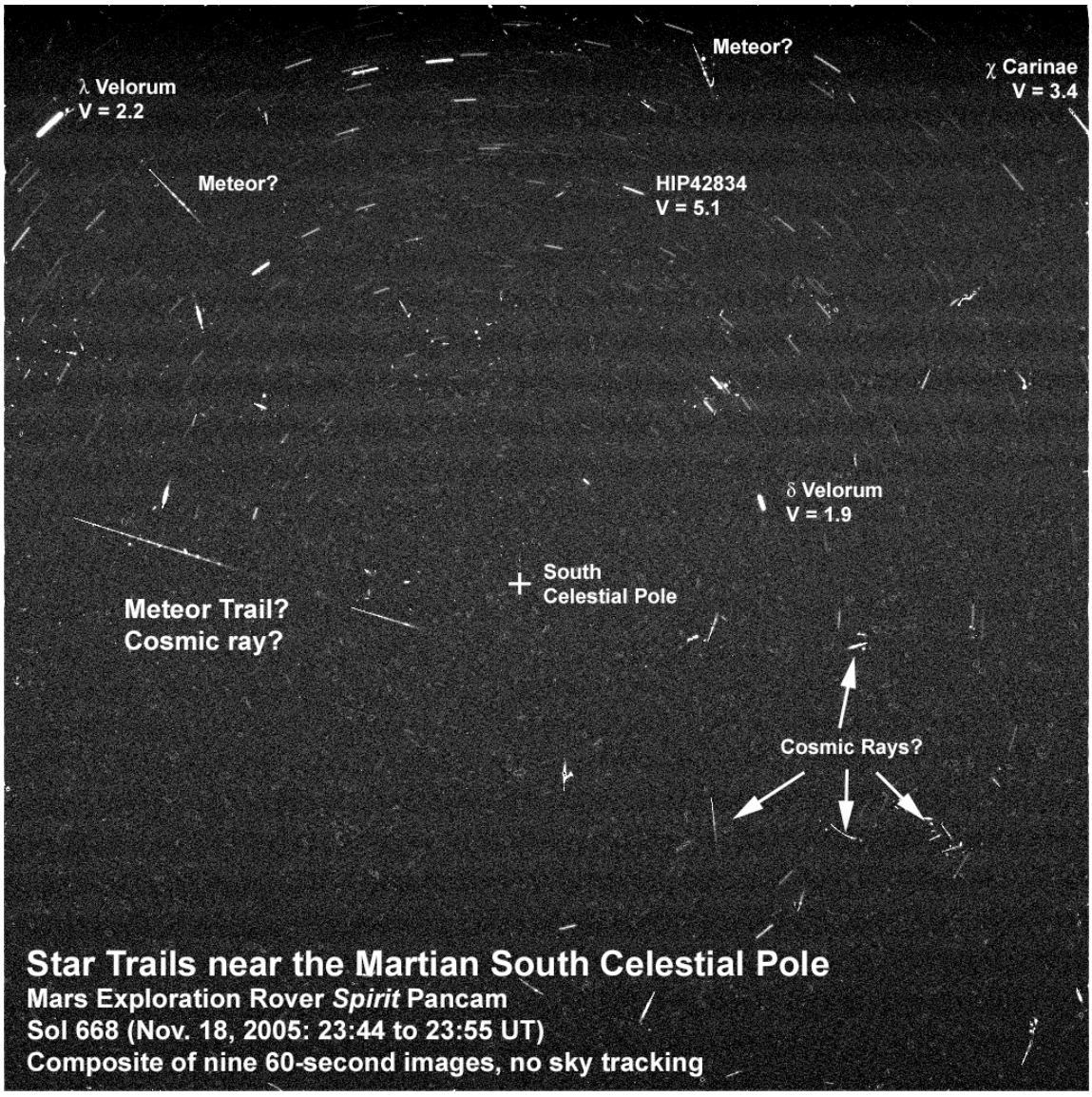

Figure 9: Annotated Meteor Search Images. Image credit: NASA/JPL/Cornell

Sol	Stars Observed	Sequence ID	# of Used Images	LTST
67	ζ Ori, α Ori	P2735	3	2:02
607	AE Cet, β Cet	P2735	7	1:00
632	β Eri, β Ori, δ Ori, ι Ori, ε Ori, ζ Ori, κ Ori, η Ori, γ Ori, μ Gem, ε Gem	P2748, P2749	3, 3	00:44
643	α Eri, α Hyi, β Phe, ν Oct, ε Oct*	P2733, P2734	2, 8	21:54
647	α Eri, α Hyi, ν Oct, ε Oct*	P2739, P2740	2, 8	21:53
664	α Tau, η Tau*, δ Tau, γ Tau, ε Tau, v971 Tau*, θ^1 Tau*,θ^2 Tau*, γ^1 And*, θ Per	P2731, P2732	4, 8	1:20
666	α UMi	P2736	10	3:28
667	α Leo, γ^1 Leo*	P2738	10	2:50
668	λ Vel, δ Vel, o^1 CMa*, o^2 CMa*, ε CMa, σ CMa, δ CMa, ξ Pup*	P2741, P2742	10, 9	1:51
687	ε Tau, θ^1 Tau*, α Tau	P2730	2	4:07
694	γ Hyi, R Dor*, β Dor, α Ret, β Ret, δ Ret, β And	P2741	5	22:38
1941	β And, ω And	P2731	3	2:13
1949	α Car	P2740	5	22:06

Table 1: All Stars Observed. The * indicates that while the star was observed and data obtained, the stars was ruled out as not being useful for optical depth measurements (see Rejecting Stars and Data Points section in Chapter 3). The LTST is the time of the first image used in the sequence. For more information on sequence ID, see the Data Availability section.

Data Availability

All images used in this thesis are from the Planetary Data System (PDS), which archives spacecraft data. The PDS data set identifier is "MER2-M-PANCAM-2-EDR-V1.0" and the data set name is "MARS EXPLORATION ROVER 2 PANORAMIC CAMERA V1.0" (Lemmon, 2004).

Pancam images have a product identification (PRODUCT_ID) that includes a sequence identifier, a spacecraft clock time at the time of image acquisition, and site and location identifiers. A generic PRODUCT_ID would then read as 2PnnnnnnnnnEFFaaaappppppL1M1. The 9 'n's stand for the spacecraft clock value, the aaaa stands for the location identifier, and ppppp stands for the sequence.

The sequence identifiers for the respective nighttime optical depth imaging sets are located in Table 1. EFF indicates that it is a full frame image. Some images used in this analysis were ESF, which stands for subframed images. L1 indicates the image was using the L1 Pancam filter.

An example of a PRODUCT_ID used for nighttime optical depth measurements is 2P185272713EFFAJB1P2731L1M1, where the spacecraft time is 185272713, EFF indicates a full frame image, AJB1 is the location identifier, P2731 is the sequence identifier, and L1 is the filter used.

CHAPTER III

METHODS

Overview

In this chapter, I explain the calibration of the images, the process of star identification and the process of obtaining flux. After that I discuss the reasoning behind rejecting some stars. Next I explain the flux calibration process and how I calculated the nighttime optical depth values from the obtained star fluxes.

The images used in this analysis were not captured with the intent of being used for nighttime optical depth measurements. Thus, the analysis was performed with the intent of verifying these images as valid for nighttime optical depth measurements, and once verified as valid, to look for any significance in the results that may indicate nighttime clouds or fogs.

Reading & Calibration of Data

The program that obtained star fluxes was written in the Interactive Data Language (IDL). The first step was to obtain information from the PDS labels attached to the star images that was relevant for image analysis. This included instrument azimuth and elevation angles, a description of the rover's orientation and the camera's focal plane geometry, exposure duration, sol number, and LTST. The image exposure times

were checked, and if the image exposure length was less than eight seconds long, the image was rejected. Below eight seconds of exposure time, the stars did not have a sufficient signal-to-noise ratio to obtain useful flux, and thus the images were not analyzed.

Nighttime optical depth images were analyzed in pairs. One image was used for background (mostly electronic bias) subtraction. The background images were at an equal or lower exposure time. In most cases, the first image in each sequence was used as the background subtraction image for all images in a given sequence. The rest of the images used the first image in a given sequence that had a sufficient exposure length. The purpose of the image subtraction was to remove electronic bias and readout dark current. The electronic bias gives images of pure black an approximately 20 DN signal, so this must be corrected for. The readout dark current is approximately a few DN and varies across the image; it accumulates during the CCD readout from the inactive part of the CCD. The temperature of the CCD impacts the background value, shifting the bias as the CCD warms. In all images, the two pixel columns closest to the left and right edges were removed due to CCD readout artifacts interfering with the average background DN.

When including the background image in the visual analysis of each pair, the star trails are apparent across the two images. This pairing allowed cosmic rays to be visually identifiable as random noise.

Star Identification & Obtaining Flux

Among the information provided in the PDS label is a geometric model that determines the projection of any pixel onto the sky or surface. This information was coupled with *The Astronomical Almanac Online*'s 2008 bright star list (BSL) produced by the U.S. Naval Observatory and H.M. Nautical Almanac Office, which allowed for the creation of a model of how the sky should appear.

The BSL provides the location of stars in right ascension (RA) and declination (dec), which are azimuth and elevation angles in a coordinate system oriented to Earth's rotational axis and spring equinox. In addition, it provides the magnitude of the stars through a common "visual" filter (*V*), color differences of the blue and visual magnitudes (*B*-*V*), and notes about the stars.

Upon reading in the star list, the photometric system was changed from the standard *V* band to the Pancam L1. Flux (F_e) is proportional to 2.512^{-V}; specifically, the flux in W m-2 nm-1 (the Pancam calibration system) is given by

$$F_e = \frac{(3640 \cdot 1\times10^{-26} \cdot c)}{(0.55\times10^{-6})^2 / 1\times10^{9}} \times 2.512^{-V} \quad (1)$$

where *c* is the speed of light in m/s. The effective temperature of a star is estimated as

$$T_{eff} = \frac{(8540K)}{(B-V)+0.865} \quad (2)$$

Given an effective temperature and V-band flux, the spectrum is uniquely constrained, and then averaged over the longer wavelength Pancam L1 band. Thus, all stars were converted from V magnitudes to L1 fluxes. A final conversion used the Bell et al., 2003 calibration to convert fluxes into DN/s.

The second conversion necessary for the stars was geometric. An existing tool to convert RA and dec to local azimuth and elevation was used for the beginning and end of each exposure. The camera geometric information was used to convert azimuth and elevation to pixel coordinates. A mask was drawn to include all pixels within a four pixel range of the line segment connecting beginning and end. Generally speaking, the rover's attitude is not sufficiently well known that the stars in the model would align with those in the image. As such, the model was shifted in azimuth (yaw) and elevation (pitch) and was rotated (roll) to maximize the flux that fell into the total set of star masks for an image. At this point the image was visually inspected using red to show the masks superimposed on the image (Figs. 10, 11). Manual adjustments were made if needed.

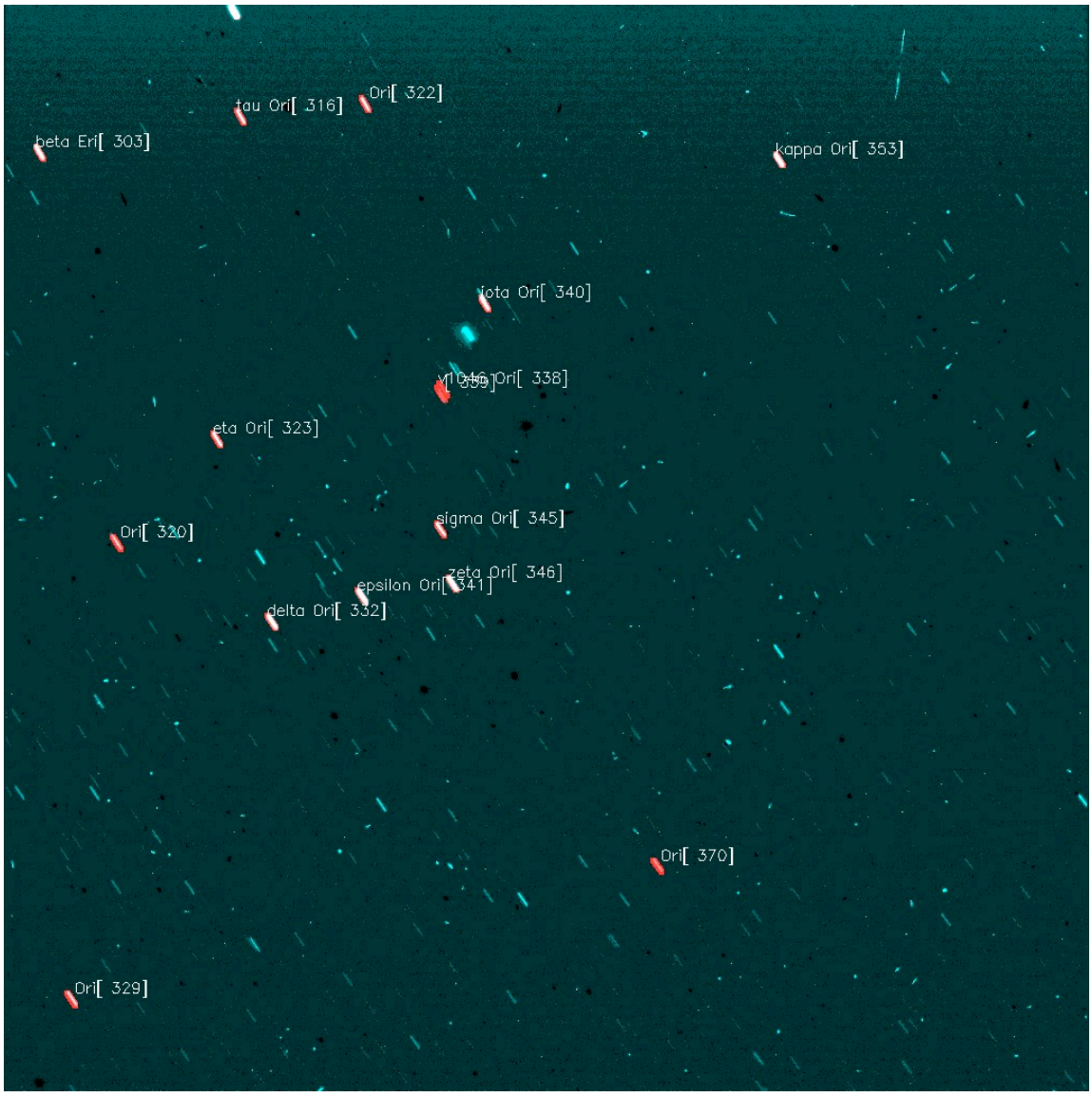

Figure 10: Processed Nighttime Image Example #1. This is of the constellations Orion and Eridanus on sol 632.

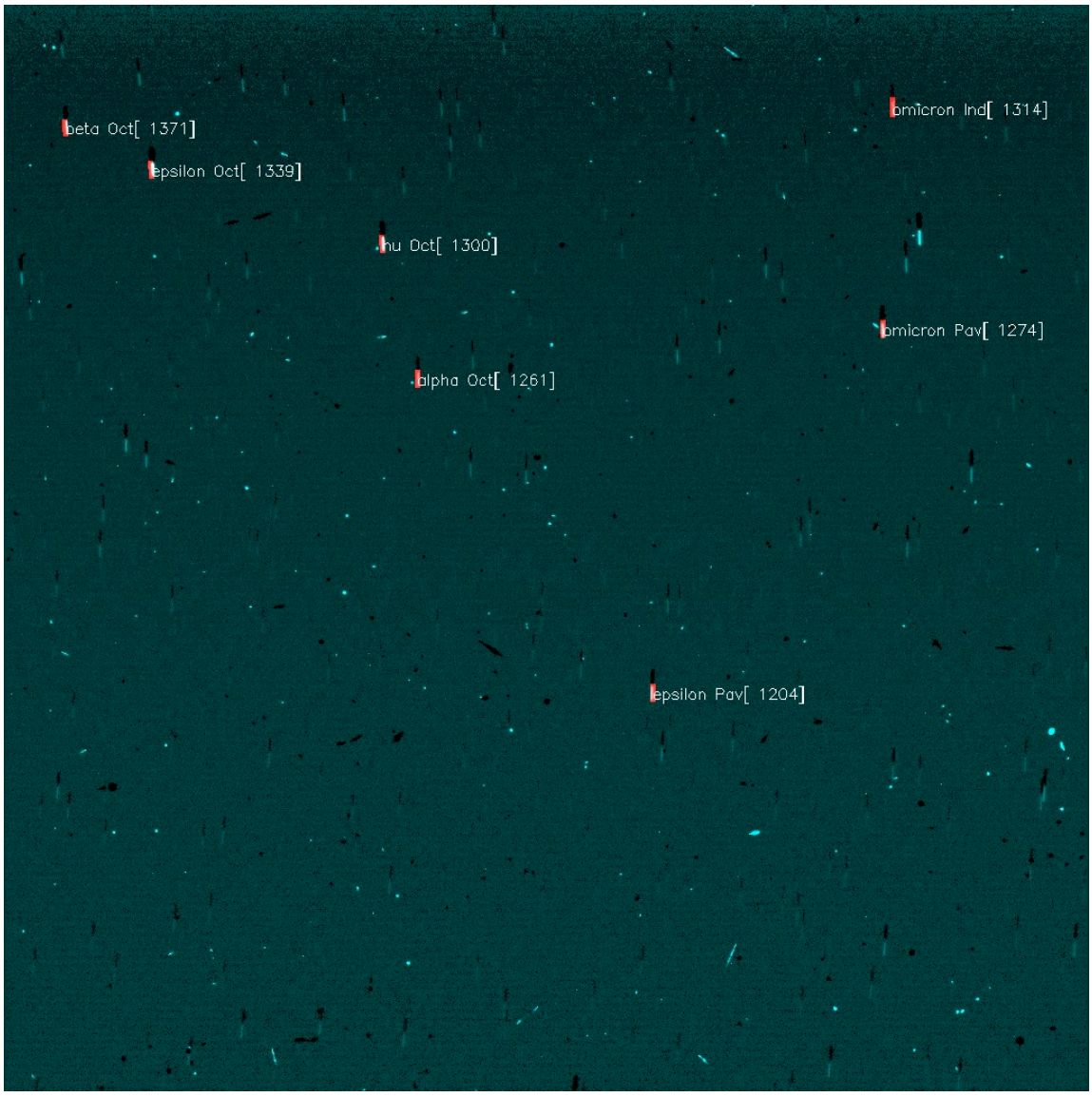

Figure 11: Processed Nighttime Image Example #2. This is of the constellations Octans, Pavo, and Indus on sol 643.

Finally, the observed star flux (F_o) was determined by measuring the background DN by averaging pixels immediately adjacent to the star mask, subtracting the background from all pixels in the mask, summing the DN in the mask, and dividing by the exposure time. Thus, the raw measurement ends up as accumulated DN/s.

The images used in this data set were taken at various elevation angles. The elevation angle affects the flux since the incoming star flux would have different path lengths through the atmosphere. As the path length through the atmosphere increases, attenuation also increases. This difference in path length necessitates the need to calculate a baseline flux ratio assuming a zenith view. The flux ratio (*FR*) is defined as the observed star flux divided by the expected star flux. A zenith view has the shortest path length through the atmosphere, which allows for the least atmospheric extinction to occur.

Rejecting Stars & Data Points

Each pair of images was displayed and manually inspected for any anomalies, such as cosmic ray interference or mask overlap between close stars. Any stars that had visible flaws were excluded from further analysis.

Variable stars were also closely inspected. If the brightness of a particular variable star varied by less than 5% in magnitude, then the variable star was kept in the analysis and the variability added into the observed flux error for that star. Variable stars salvaged include β Orion and δ Orion. Variable stars with more than 5% variation in star magnitude, such as R Doradus, were excluded from nighttime optical depth calculations.

The program's mask combined with Pancam's low resolution CCD is problematic for optical double and binary or multiple star systems. Some additionally excluded stars were stars that, while not in binary systems, were too close for Pancam

and the mask to distinguish with enough fidelity for accurate flux measurements. Some stars had masks that overlapped due to the exposure length. Overlapping stars were excluded, and binary star systems were excluded if their combined flux was not reliably determined.

Around *Spirit* sol 1270, a global dust storm occurred which caused a significant accumulation of dust on the Pancam lens. There were a few nighttime images taken after this global dust storm, however there were not enough images taken of bright stars to allow for an independent star flux ratio calibration, but were still analyzed using a flux ratio calibration from daytime optical depth values. These stars have more error in their nighttime optical depth measurements as a result.

Spirit took daily optical depth measurements via Sun imaging. A baseline nighttime star flux (F_{test}) was calculated using the daytime optical depth value (τ) and expected flux value calculated in the previous section such that

$$F_{test} = F_e \cdot e^{-\tau * \eta} \tag{3}$$

where η is the airmass factor. The airmass factor describes the direct optical depth path length through the atmosphere. The airmass factor is calculated by

$$\eta = \frac{1}{\sin(\theta)} \tag{4}$$

where θ is the individual star elevation angle, which is accurate for plane parallel atmosphere and is accurate for Mars down to 10 degree elevation angles given the dust scale heights measured by Lemmon et al., 2004.

To identify any potential bad stars left after the exclusions described earlier in this section, a metric was calculated by dividing the baseline nighttime star flux by the observed star flux. If the resulting metric was between 0.25 and 4, the star was marked as good for nighttime optical depth calculations. This was the simplest method to identify covert binaries and variables in preliminary work. Only three observations were marked bad, leaving a total of 146 star observations useful for calculating nighttime optical depth.

Flux Calibration

To calibrate all of the flux ratios (observed star flux divided by expected star flux) necessary for nighttime optical depth calculations, a flux ratio assuming a zenith view needed to be calculated. The flux ratio here is calculated as the ratio of the observed flux to the expected flux. The flux ratio error FR_{er} is calculated

$$FR_{er} = \ln(1 + \frac{F_{o,er}}{F_o}) \tag{5}$$

where $F_{o,er}$ is the observed flux error, calculated from DN uncertainties in the background pixels and star magnitude errors.

A flux ratio calibration is needed due to the fact that Pancam was calibrated for landscape imaging, not aperture photometry (i.e., the integration of flux over some spatial aperture, as is done via the star masks). The BSL stars' fluxes were converted to DN/s using the Bell et al., 2003 calibration, which was derived for diffuse sources (i.e., a landscape) using an integrating sphere. The calibration for a point source is likely to be different: if 10, 20, or 50% of the light from a point source is scattered many pixels to a few degrees away, that light counts in the diffuse measurement but is omitted in the point source (or aperture) measurement. Thus, I derive a calibration of the L1 filter for point sources following the same method, applied to stars, as has been used for day time measurements with the Sun. On each day, the flux was modeled as following Beers' Law (i.e., Equ. 3). The model was implemented as a linear fit of the natural log of the flux ratio as a function of airmass. An example linear fit is shown in Figure 12. The fit results in an estimate of optical depth, which is discarded. It also resulted in an estimate of what the flux ratio is without any atmosphere (the intercept of the natural log of the flux ratio with zero airmass). The set of independent estimates of the intercept are shown in Table 2.

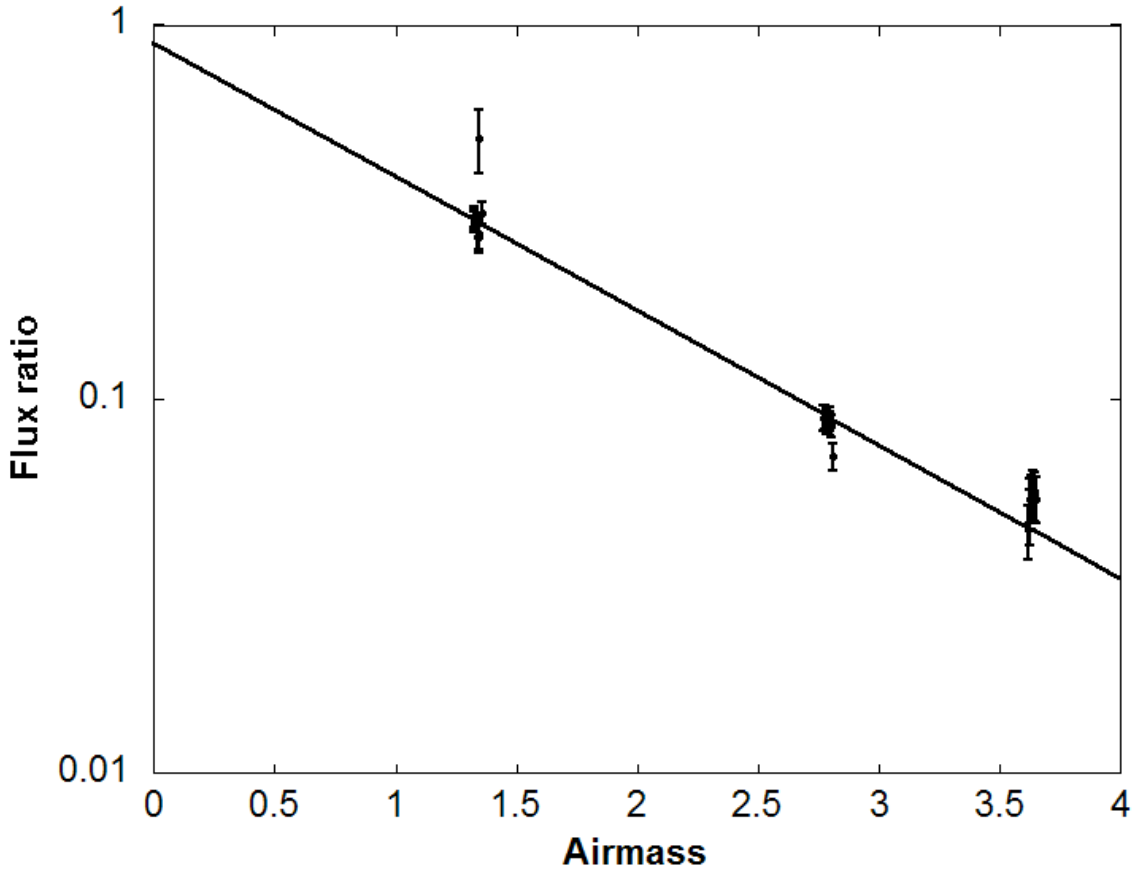

Figure 12: Sol 668 Data with Beers' Law Fit. All data from sol 668 are shown with 1-sigma error bars. The line is the fit described in the text, converted into flux/ratio space (i.e., from a linear fit to an exponential). The intercept (-0.11 ± 0.02) is close to the overall best intercept of -0.10 ± 0.02.

Sol	Linear Fit Intercept (IN)	Standard Deviation (σ)
67	0.454046	0.345404
607	18.1299	25.1072
632	-0.105816	0.116027
644	0.175021	0.118338
648	-0.0206303	0.109369
664	-1.55104	0.245623
666	0.289770	1.81293
667	-0.134550	1.33770
668	-0.118281	0.0238403
687	2.31740	1.56311
695	-0.123375	0.201608
1941	289.978	49.5169
1950	-23.7550	1.97735

Table 2: Linear Fit Results.

To get the baseline flux ratio assuming a zenith view to use for flux ratio calibration, a weighted average of all good intercept data was calculated. Sol 664's data was excluded from the weighted average calculation due to not passing the linear fit check. All of the sols after the global dust storm around sol 1270 were also excluded from the weighted average. All other data was included for this baseline flux ratio.

To calculate the weighted average, a standard weighted average formula was used such that

$$\underline{FR} = \Sigma \frac{IN / \sigma^2}{1 / \sigma^2} \tag{6}$$

where $\underline{FR}$ is the flux ratio weighted average including accumulated error, IN is the linear fit intercept, and σ is the standard deviation. This weighted average is turned into the baseline flux ratio assuming a zenith view (FR_0) by e to the $\underline{FR}$ power. The baseline FR_0

error ($FR_{0,er}$) was calculated by the weighted average of the accumulated error from all of the good intercept points. The overall best intercept is -0.10 ± 0.02, which implies that small aperture photometry captures 10% less flux than imaging a diffuse source (i.e., infinite aperture).

This baseline flux ratio can then be used to calibrate all data points to account for the fact all of the stars imaged have different path lengths through the atmosphere. There is now enough information to calculate the nighttime optical depths using the Beer-Lambert Law

$$FR = FR_0 \cdot e^{\tau \cdot \eta} \tag{7}$$

which compares the stellar radiation attenuation to the atmospheric properties through which the radiation is traveling.

Determining Nighttime Optical Depth

In this thesis, the nighttime optical depth (τ_N) was calculated using the following form of the Beer-Lambert law

$$\tau_N = -\ln\left(\frac{FR}{FR_0}\right) \cdot \frac{1}{\eta} \tag{8}$$

The nighttime optical depth error ($\sigma_{\tau,N}$) was calculated as the flux ratio error multiplied by one over the airmass factor. The cumulative nighttime optical depth error ($\sigma_{\tau,N,tot}$) calculated as

$$\sigma_{\tau,N,tot} = \sqrt{FR_{0,er}^2 + (0.05 \cdot \tau_N)^2 + \sigma_{\tau,N}^2} \quad (9)$$

A 5% uncertainty was quadratically added into the nighttime optical depth error as described in Lemmon et al. 2004 reflecting short timescale and length-scale variations in optical depth: the optical depth for any given line of sight is only within ~5% of the average optical depth due to random physical variations. The baseline flux ratio error and the flux ratio error multiplied by the airmass factor were also combined into this cumulative nighttime optical depth error.

A weighted average was also calculated for each individual sol to be able to compare overall nighttime optical depth to the overall daytime optical depth. Each night ranged from having two to 35 valid data points. Each sol's nighttime optical depth weighted average, τ_{sol}, was calculated using normal weighted averaging including accumulated error. The resulting sol weighted average nighttime optical depths were compared against the respective sol's daytime optical depth values (Table 3).

Sol	τ_N	$\sigma_{\tau,N,tot}$	τ	σ_τ	Night vs. Day Difference	Night vs. Day σ
67	0.5439	0.0199	0.7083	0.0354	-0.1644	0.0406
607	1.1518	0.0958	0.6441	0.0322	0.5077	0.1010
632	0.5466	0.0133	0.6066	0.0303	-0.0600	0.0331
644	0.6167	0.0226	0.6865	0.0343	-0.0698	0.0411
648	0.6248	0.0233	0.6538	0.0327	-0.0289	0.0402
664	0.8029	0.0213	0.7729	0.0386	0.0300	0.0441
666	0.7797	0.0240	0.7674	0.0384	0.0123	0.0453
667	0.7420	0.0191	0.767	0.03835	-0.025	0.0429
668	0.8222	0.0097	0.7703	0.0385	0.0520	0.0397
687	0.7404	0.0318	0.7841	0.0392	-0.0437	0.0505
695	0.7225	0.0198	0.7160	0.0358	0.0065	0.0409
1941	0.7657	0.0346	0.6573	0.0329	0.1085	0.0477
1950	0.7622	0.0218	0.5772	0.0289	0.1849	0.0361

Table 3: All Sol Averaged Results.

CHAPTER IV

DISCUSSION

Comparison Between Daytime & Nighttime Optical Depth

Optical depth varies over the Martian seasons (Fig. 13). These variations, as seen by *Spirit*, were described initially by Lemmon et al., 2004 and there is a substantially updated description in Lemmon et al., 2013 (manuscript in review). The daytime optical depth values have been archived to the PDS on a quarterly basis (Lemmon, 2004). The first nighttime imaging campaign in the sol 600s occurred when daytime optical depth values were between 0.6 and 0.8. The second nighttime imaging campaign in the sol 1900s occurred when daytime optical depth values were between 0.6 and 0.7. One additional image set was used from sol 67, where the daytime optical depth value was approximately 0.7. In general, the Martian atmospheric daytime optical depth values range between 0.2 and 1.0, with exceptions during major dust storm events (Lemmon et al., 2004, 2013). The lower optical depths are associated with the southern hemispheric winter, and more importantly, with the time Mars is near aphelion. Thus insolation is actually maximized during the intermediate optical depths that represent the clearest times of southern hemispheric summer.

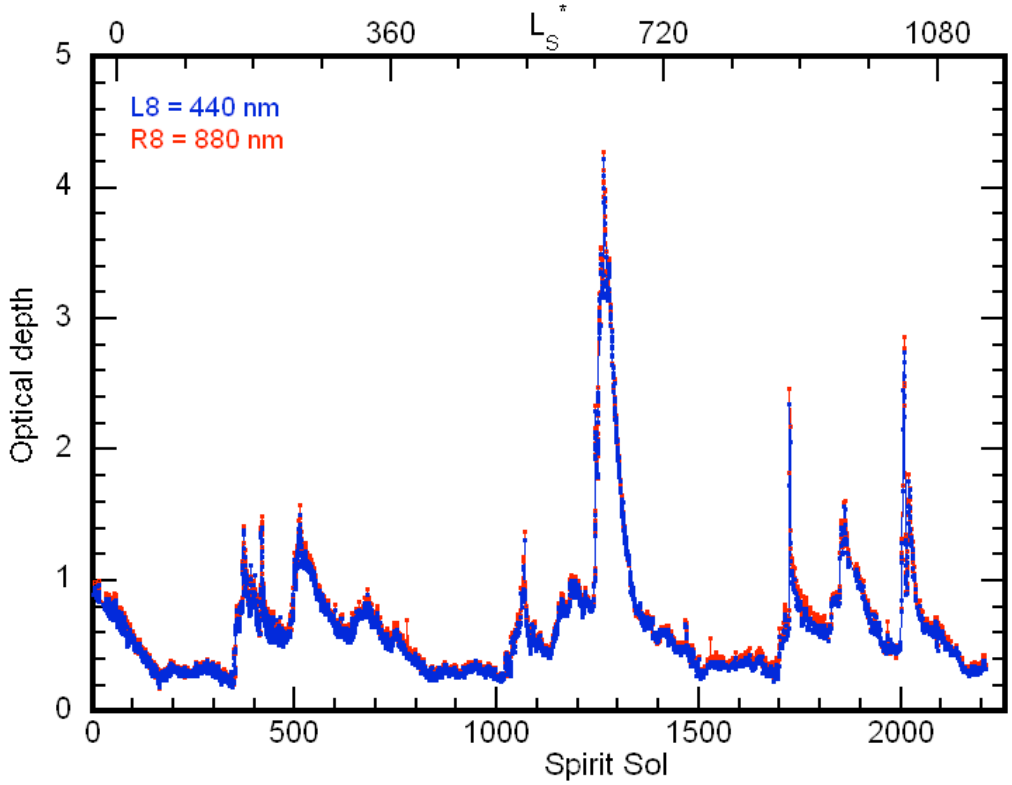

Figure 13: MER Daytime Optical Depth Record. This is the Mars Exploration Rover daytime optical depth record over the course of *Spirit*'s lifetime. Optical depth at 440nm is shown in blue while the optical depth at 880nm is shown in red. This figure is from Lemmon et al., 2013.

Once all nighttime optical depth values were calculated as shown by the methods in Chapter 3, they were compared to the daytime values. Figure 14 only shows the optical depth information between sol 600 and 700. For sols 67, 1941, and 1949, the information is provided numerically in Table 3 at the end of Chapter 3.

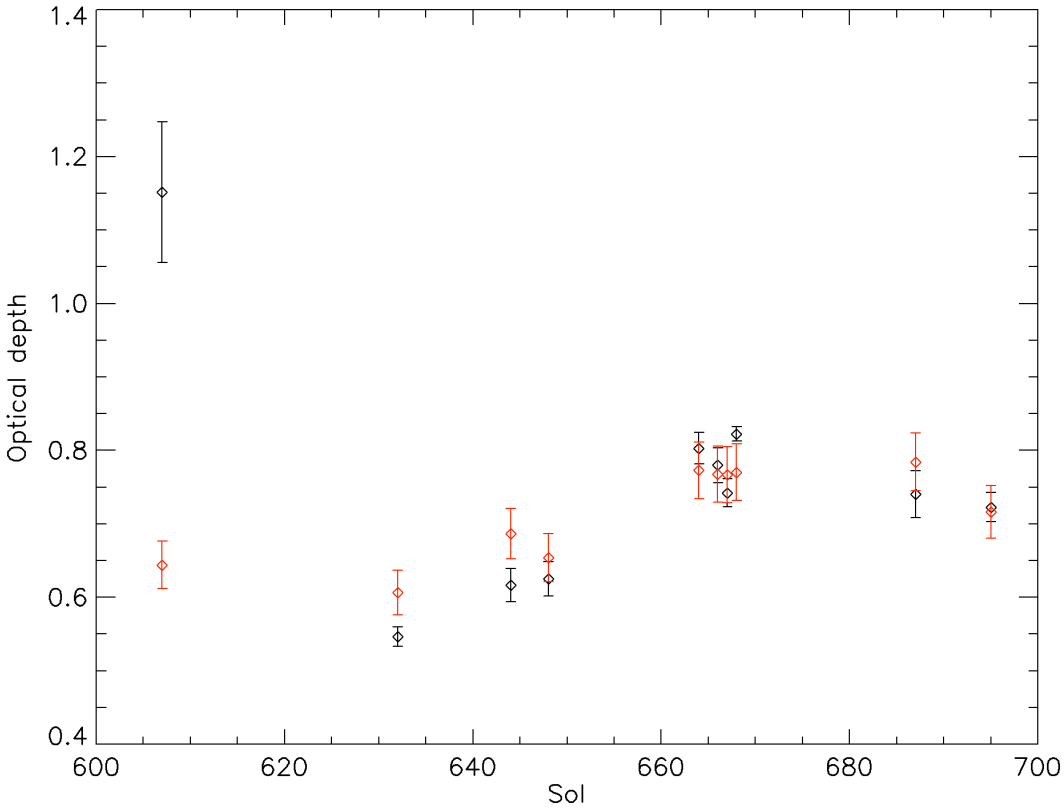

Figure 14: Sol Averaged Optical Depth. This is a graph of the weighted nighttime optical depths for the sol 600s nighttime campaign. Stars represent nighttime optical depth values and included their respective error bars. Red triangles represent daytime optical depth values. For sol 67 and 1900s values, see Table 3.

To determine if any sol averaged nighttime optical depths were statistically significant when compared to the daytime optical depth values, the following statistical tests were performed.

The first test performed was to compare the average of all subtracted differences of nighttime and daytime optical depth while still including accumulated error. The result was 0.03 ± 0.04. This indicates that overall, the sol averaged nighttime optical depth is similar to the daytime optical depth values given the associated error bars.

The values in the sol 1900s were excluded from further analysis due to the dramatic change in calibration of the camera and the fact that an independent calibration could not be performed for those sols due to the low number of good stars found in these images. Of the remaining stars, two nights were obvious outliers of a 95% confidence interval: most were within one sigma of the prediction; all but sol 67 and 607 were within two sigma; and these two outliers were each different by more than three sigma.

Sol 67 was much lower than the daytime value in a time of slowly and uniformly decreasing daytime optical depth. Sol 607 had an apparently significant increase at night. The two discrepancies are of comparable magnitude but opposite sign. It seems more likely that they represent a non-Gaussian distribution of errors rather than they show one night of clouds and one of an unknown phenomenon. Sources of non-Gaussian errors might include influence by unscreened cosmic rays not caught by previous filtering methods on the star measurements or in the background subtraction process.

It remains possible that sol 607 shows fog development at ~01:20 LTST, but the grounds for such a claim do not seem strong. It is worth noting this is close in time that Thomas et al., 1999 observed a peak in optical depth values (02:00 LTST), although the peak was within their data set's errors bars.

Small-Scale Variability

While the nighttime sol-averaged results indicated a likelihood that individual nighttime optical depths would fit within the 95% confidence level for optical depth, a

search for small-scale variability was carried out. This search would, in principle, detect discrete clouds rather than layer, which might block small parts of the sky.

In most cases, the individual measurements were consistent with the sol-averaged value to within a 95% confidence level. There were four individual observations that were identified as not being within this confidence level. This leads to 3% of the data points outside of the 95% confidence level, which is an expected amount of error and is not statistically significant. These were most likely the result of non-Gaussian errors discussed in the previous section.

These four observations were still investigated further for potential results. The observations were on different nights, and the other observations on those nights fit into the confidence levels. As described in the previous section, the errors on all but sol 607 were either minor or abstract errors. Sol 607 only had two valid data points. One data point was greater than two-sigma from the sol-averaged value, while the other data point was just inside the upper boundary of the 95% confidence level. Sol 607 has the strongest case going for having observed nighttime clouds, but is still unlikely that it is a statistically significant result, i.e., an actual cloud or fog observation.

Lessons Learned for Future Missions

Many lessons learned from this analysis can be applied towards characterizing diurnal variations of clouds with a nighttime optical depth campaign for current and

future surface missions to Mars. The major recommendations are presented, followed by how to specifically use the *Curiosity* rover for future optical depth studies.

First, the campaign should be designed to test specific predictions. GCMs can provide insight as to when clouds may form. Observations from orbiters provide insight as to when water vapor is fed to an area (generally, this is the aphelion cloud season for equatorial and tropical latitudes).

A consistent star field should be picked with as few variable and binary stars as possible. The stars selected for analysis should also be as bright as possible to allow for as much signal as possible in the CCDs. In this thesis, the star fields that provided the most useful and consistent data were those in the constellations Orion and Taurus. However, for a full year of consistent observations, constellations visible during the winter months that contain bright stars will have to be selected.

Nighttime images should have consistent exposure times. *Spirit*'s nighttime images ranged from a few seconds to several minutes. *Spirit*'s best nighttime images had exposure times between 45 seconds and one minute. Exposure times should be selected that allow for star trails to spread across multiple pixels. Images should be obtained in a minimum set of four images, but preferably up to ten images with a minimal time separation. This allows for consistency checks across images, in the case of single anomalous star.

Optimally, multiple image sets would be taken covering the entire night at a regular cadence. This would allow for full nocturnal coverage in the case of clouds or

fogs developing towards twilight or towards dawn. It would also capture clouds and fogs that result from radiative cooling at night.

Daytime optical depth measurements should be taken near noon and near sunset or sunrise on the days of the nighttime optical depth measurements. This will provide a background optical depth value to compare against any potential trends in nighttime optical depth data.

The newest addition to the Mars spacecraft family is the *Curiosity* rover, which landed in Gale Crater on Mars, on August 6, 2012. Also currently planned for future Mars exploration is a *Curiosity*-class rover to launch in 2020. The nighttime optical depth analysis carried out in this thesis can be used to assist in developing a more systematic nighttime optical depth campaign and potentially provide better constraints on any potential nighttime clouds or localized fogs.

An advantage that *Curiosity* has over *Spirit* is that *Curiosity* has a nuclear power source instead of being a solar powered mission like *Spirit* (Grotzinger et al., 2012). This means that power is less of a concern throughout the seasons and *Curiosity* would be able to obtain year-round nighttime optical depth information, instead of being limited to the summertime like *Spirit*.

The Mastcams, short for mast cameras, are the main science and remote sensing cameras on *Curiosity*. The cameras use CCDs to collect photons to make images, but the CCD is overlaid with a Bayer-pattern micro-filter set filter. Each set of 2x2 pixels has two green, one red, and one blue micro-filter, each with a broad bandpass (Ghaemi, 2009). The Mastcam images obtain color information due to the Bayer-pattern filter,

even with a blank filter similar to L1 on *Spirit*'s Pancam. The star trails will be "colorful" across multiple pixels, which may affect the observed stars fluxes. Test images should be taken of bright stars well characterized from this thesis, such as stars in the constellation Orion or Taurus, for cross-calibration.

ChemCam, short for chemical camera, may be useful for nighttime opacity information. ChemCam is a two-part instrument, made of a Laser-Induced Breakdown Spectrometer (LIBS) and a Remote Micro Imager (RMI) (Maurice et al., 2012). ChemCam has an extremely narrow field of view, but enough to view a single star. Star flux could be obtained from RMI images. ChemCam can observe radiation wavelengths between 240-850 nanometers with high precision (Maurice et al., 2012). Specific water lines could be monitored from these passive spectra observations to look for abnormally high signals of water vapor or condensates in the atmosphere.

Another instrument that can assist in looking for nighttime clouds and fogs is the Rover Environmental Monitoring Station (REMS). REMS can provide pressure, humidity, ultraviolet radiation, wind speed and direction, air temperature, and ground temperature information (Gómez-Elvira et al., 2012). In Wilson et al., 2007, they saw a thermal anomaly at night that GCMs indicated were a result of nighttime clouds trapping infrared radiation, as discussed in Chapter 1. With the ability to monitor all of these weather conditions, it would aid in further research to also obtain temperature information while taking nighttime images. This temperature information can be correlated back to the nighttime optical depth information if any anomalously warm nights occur as additional evidence for or against nighttime clouds or fogs.

With the lessons learned from *Spirit*'s nighttime imaging campaigns, *Curiosity* will be able to carry out a comprehensive nighttime atmospheric optical depth campaign over several Martian years to gain a complete understanding of any potential changes in atmospheric optical depth over the full diurnal and annual scale. This will provide added constraints to the dust and water cycles of Mars.

CHAPTER V

CONCLUSIONS

Nighttime images taken by *Spirit* over the course of the mission have been shown as useful for obtaining nighttime optical depth. The stars processed provided optical depths similar to daytime optical depths, within uncertainty, even though many of the images were not designed for this purpose.

The nighttime sol-averaged results align closely with the daytime optical depth values when optical depth error, observed star flux error, and a 5% error for localized, short-term variations as described in Chapter 3. Each of the 13 sols ranged from having two to 35 valid data points per sol. With only 13 sols of valid data in the southern hemispheric summer and a lack of temporal and seasonal variability, there is not any insight to trends on a longer timescale from this data set.

While there is no strong evidence of clouds, this thesis does not rule out the possibility of nighttime clouds or fogs, especially given the extensive literature on the subject discussed in Chapter 1. Four stars were identified outside of the 95% confidence interval for nighttime optical depth, however this was only 3% of the total nighttime data and thus within acceptable levels of error and unlikely to be the result of localized nighttime clouds or fogs. Sol 607 was the closest to providing evidence for a nighttime water condensate observation. Sol 607 had only two valid data points, with one significantly outside and one just inside the upper boundary of the 95% confidence level. However, these outliers including sol 607 were likely the result of non-Gaussian errors.

Many lessons learned from this analysis can be applied towards current and future Mars missions, such as *Curiosity*, to better constrain nighttime optical depth values and potentially provide insight into any localized cloud or fog formation. Consistency and intent are the main keys to a future nighttime optical depth campaign. Using GCMs, optimal times for nighttime cloud or fog formation should be used for planning nighttime optical depth observations. Major recommendations are picking a consistent, bright star field with as few variable and binary stars as possible; choosing an exposure time that allows for sufficient star flux to be observed while minimizing cosmic ray influences; imaging sets timed to cover the complete nocturnal cycle; obtaining a minimum of four images at a time to allow for consistency checks across image sets; and obtaining daytime optical depths to provide context for the nighttime optical depth values.

REFERENCES

Bell JF, III, Squyres SW, Arvidson RE, et al (2004) Pancam Multispectral Imaging Results from the Spirit Rover at Gusev Crater. *Science* 305(5685): 800-806.

Bell JF, III, Squyres SW, Herkenhoff KE, et al (2003) Mars Exploration Rover Athena Panoramic Camera (Pancam) investigation. *Journal of Geophysical Research: Planets* 108(E12): 1703-1709.

Cantor B, Malin M, and Edgett KS (2002) Multiyear Mars Orbiter Camera (MOC) observations of repeated Martian weather phenomena during the northern summer season. *Journal of Geophysical Research: Planets* 107(E3): 1-8.

Clancy RT and Sandor BJ (1998) CO_2 ice clouds in the upper atmosphere of Mars. *Geophysical Research Letters* 25(4): 489-492.

Colburn DS, Pollack JB, and Haberle RM (1988) Diurnal variations in optical depth at Mars. *Icarus* 79(1): 159-189.

Domokos A, Bell JF, III, Brown P, et al (2007) Measurement of the meteoroid flux at Mars. *Icarus* 191(1): 141-150.

Ghaemi FT (2009) Design and fabrication of lenses for the color science cameras aboard the Mars Science Laboratory rover. *Optical Engineering* 48(10): 103002.

Gómez-Elvira J, Armiens C, Castañer L, et al (2012) REMS: The Environmental Sensor Suite for the Mars Science Laboratory Rover. *Space Science Review* 170(1-4): 583-640.

Greeley R, Whelley PL, Arvidson RE, et al (2006) Active dust devils in Gusev crater, Mars: Observations from the Mars Exploration Rover Spirit. *Journal of Geophysical Research: Planets* 111(E12): S09.

Grotzinger JP, Crisp J, Vasavada AR, et al (2012) Mars Science Laboratory Mission and Science Investigation. *Space Science Review* 170(1-4): 5-56.

Haberle RM and Jakosky BM (1991) Atmospheric effects on the remote determination of thermal inertia on Mars. *Icarus* 90(2): 187-204.

Hanel R, Conrath B, Hovis W, et al (1972) Investigation of the Martian environment by infrared spectroscopy on Mariner 9. *Icarus* 17(2): 423-442.

Kahn RA, Martin TZ, Zurek RW, and Lee SW (1992) *The Martian Dust Cycle*. In: *Mars*. Tucson: University of Arizona Press, 1017-1053.

Lemmon MT (2004) MER Mars Pancam Atmospheric Opacity RDR V1.0, NASA Planetary Data System, MER1/MER2-M-PANCAM-5-ATMOS-OPACITY-V1.0.

Lemmon MT, Wolff MJ, Bell JF, III, Cantor B, Smith MD, and Smith PH (2013) The Visible Atmospheric Optical Depth Record of 3 Mars Years of the Mars Exploration Rover Mission. *Journal of Geophysical Research: Planets,* in review.

Lemmon MT, Wolff MJ, Smith MD, et al (2004) Atmospheric Imaging Results from the Mars Exploration Rovers: Spirit and Opportunity. *Science* 306(5702): 1753-1756.

Malin MC, Calvin WM, Cantor BA, et al (2008) Climate, Weather, and North Polar Observations from the Mars Reconnaissance Orbiter Mars Color Imager. *Icarus* 194(2): 501-512.

Malin MC, Edgett KS, Cantor BA, et al (2010), An Overview of the 1985-2006 Mars Orbiter Camera Science Investigation. *International Journal of Mars Science and Exploration*, 4: 1-60.

Maurice S, Wiens RC, Saccoccio M, et al (2012) The ChemCam Instrument Suite on the Mars Science Laboratory (MSL) Rover: Science Objectives and Mast Unit Description. *Space Science Review* 170(1-4): 95-166.

Möhlmann DTF, Niemand M, Formisano V, Savijärvi H, and Wolkenberg P (2009) Fog Phenomena on Mars. *Planetary and Space Science* 57(14-15): 1987-1992.

Montmessin F, Forget F, Rannou P, Cabane M, and Haberle RM (2004) Origin and role of water ice clouds in the Martian water cycle as inferred from a general circulation model. *Journal of Geophysical Research: Planets* 109(E10): 10-29.

Moores JE, Komguem L, Whiteway JA, Lemmon MT, Dickinson C, and Daerden F (2011) Observations of near-surface fog at the Phoenix Mars landing site. *Geophysical Research Letters* 38(L04): 203.

Richardson MI, Wilson RJ, and Rodin AV (2002) Water ice clouds in the Martian atmosphere: General circulation model experiments with a simple cloud scheme. *Journal of Geophysical Research: Planets* 107(E9): 1-29.

Rodin AV, Clancy RT, and Wilson RJ (1999) Dynamical properties of Mars water ice clouds and their interactions with atmospheric dust and radiation. *Advances in Space Research* 23(9): 1577-1585.

Smith MD (2004) Interannual Variability in TES Atmospheric Observations of Mars During 1999-2003. *Icarus* 167(1): 148-165.

Smith MD, Pearl JC, Conrath BJ, and Christensen PR (2001) Thermal Emission Spectrometer Results: Mars Atmospheric Thermal Structure and Aerosol Distribution. *Journal of Geophysical Research: Planets* 106(E10): 23929-23945.

Smith PH and Lemmon MT (1999) Opacity of the Martian Atmosphere Measured by the Imager for Mars Pathfinder. *Journal of Geophysical Research* 104(E4): 8975-8985.

Smith SA and Smith BA (1972) Diurnal and seasonal behavior of discrete white clouds on Mars. *Icarus* 16(3): 509-521.

Svitek T and Murray B (1990) Winter frost at Viking Lander 2 site. *Journal of Geophysical Research* 95(B2): 1495–1510.

Thomas N, Britt D, Herkenhoff K, Murchie S, Semenov B, Keller H, and Smith P (1999) Observations of Phobos, Deimos, and bright stars with the Imager for Mars Pathfinder. *Journal of Geophysical Research* 104(E4): 9055-9068.

Toon OB, Pollack JB, and Sagan C (1977) Physical properties of the particles composing the Martian dust storm of 1971-1972. *Icarus* 30(4): 663-696.

Wall SD (1981) Analysis of condensates formed at the Viking 2 lander site: The first winter. *Icarus* 47(2): 173-183.

Whiteway JA, Komguem L, Dickinson C, et al (2009) Mars Water-Ice Clouds and Precipitation. *Science* 325(5936): 68-70.

Wilson RJ, Neumann GA, and Smith MD (2007) Diurnal variation and radiative influence of Martian water ice clouds. *Geophysical Research Letters* 34(2): 7-10.

APPENDIX

DIFFERENCES IN UNDERGRADUATE VS. GRADUATE THESIS

In 2010, I completed an undergraduate thesis as part of the Texas A&M University Undergraduate Research Scholars program. While both this master's thesis and the undergraduate thesis cover similar material, the master's thesis is more in depth and robust.

The analysis is entirely new. A new method of image analysis was done that allowed for many more stars to be included in the analysis and for the flux to be measured with much better accuracy. The error analysis is new to this work. The derivation of the L1 filter calibration and its application to measuring optical depth is also new to this work.